High efficiency, high-resolution multiple monochromatic imaging based on multilayers mirrors array for laser-plasma diagnostic of X-ray continuum emission

Tongzhou Li[1,2], Huiyao Du[1,2], Zhong Zhang[1,2], Zhe Zhang[1,2], Qiushi Huang[1,2,4], Shengzhen Yi[1,2,*], Zhanshan Wang[1,2], Wei Wang[3,], Jinren Sun[1,2,3,***]**

[1]*MOE Key Laboratory of Advanced Micro-Structured Materials, Tongji University, Shanghai, 200092, China*

[2]*School of Physics Science and Engineering, Tongji University, Shanghai, 200092, China*

[3]*Shanghai Institute of Laser Plasma, CAEP, P.O. Box 919-988, Shanghai, 201800, China*

[4]*Zhejiang Tongyue Optical Technology Co., Ltd, Huzhou, Zhejiang, 313199, China*

[*]Email: 023123@tongji.edu.cn

[**]Email: wei_wang@fudan.edu.cn

[***]Email: sunjinren@263.net

Abstract The measurement of X-ray continuous emission from laser-driven plasma was achieved through multiple monochromatic imaging utilizing a multilayers mirrors array. This methodology was exemplified by the development of an eight-channel X-ray imaging system, capable of operating in the energy range of several keV with a spatial resolution of approximately 3 μm. By integrating this system with a streak camera, the temperature and trajectory of imploding capsules were successfully measured at the kJ-class ShenGuang III prototype laser facility. This approach provides a synchronous diagnostic method for the spatial, temporal, and spectral analysis of laser-driven plasma, characterized by its high efficiency and resolution.

This peer-reviewed article has been accepted for publication but not yet copyedited or typeset, and so may be subject to change during the production process. The article is considered published and may be cited using its DOI.

10.1017/hpl.2024.30

Key words: plasma diagnostics, multiple monochromatic imaging, X-ray continuum emission, high resolution, multilayers mirrors array

https://doi.org/10.1017/hpl.2024.30 Published online by Cambridge University Press

I. INTRODUCTION

The measurement of continuous X-ray emission from laser-driven plasma plays a crucial role in acquiring plasma information. This method becomes particularly effective at high X-ray energies, allowing for the deduction of electron temperature by analyzing the intensity ratio of the continuous spectrum independently of the electron density. Its application spans various domains of inertial confinement fusion, including laser fusion and Z-pinch, as well as magnetic confinement fusion [**Error! Reference source not found.**-2]. Current methodologies predominantly comprise transmission-type Ross filters [4], and diffraction-type gratings or crystals used in spectroscopy [5-8]. While Ross filters are simple and reliable, they offer limited spectral resolution. Conversely, diffraction-based methods provide high spectral resolution and an extensive dataset for analysis but struggle to deliver spatial resolution and are hampered by low signal intensity. Consequently, these methods are less effective in scenarios characterized by weak X-ray radiation or low electron temperatures.

The multiple monochromatic imager, another diffraction-based, multispectral imaging approach, has seen deployment at the U.S. OMEGA laser facility [9,10]. This method involves the initial imaging of continuous X-ray emissions through a pinhole array, followed by the selection of specific X-ray energies via a multilayers mirror, and the eventual capture of these monochromatic X-ray images by time-gated MCP detectors. This technique enables the extraction of spatially resolved spectral data, facilitating the analysis of electron temperature and density across different spatial and temporal dimensions. However, the limited pinhole aperture size results in low collection efficiency (approximately 10^{-8} sr) and poor spatial resolution (10–20 μm), making it a challenge to balance the signal-to-noise ratio with spatial resolution for diagnostic purposes. Thus, its use is mainly confined to the diagnostics of X-ray characteristic lines from

https://doi.org/10.1017/hpl.2024.30 Published online by Cambridge University Press

doped elements [11,12]. Given the rapid and significant variations in the temperature distribution of laser-driven plasma, a method that can more effectively measure X-ray continuous emission from plasmas, especially in the absence of dopant elements where X-ray emission is weak, becomes imperative.

This study introduces a novel multiple monochromatic imaging technique based on a multilayers mirrors array designed for the diagnostics of X-ray continuous emission within the energy range of several keVs. By employing grazing-incidence reflection to focus X-rays, this method surpasses pinhole imaging in spatial resolution, achieving 3–5 μm, and in collection efficiency, reaching 10^{-7}-10^{-6} sr [13,14]. This represents a significant advancement over previous X-ray multilayers systems [15,16], extending the operational energy range to several keVs and increasing the number of energy points from two to four. This approach facilitates the comprehensive acquisition of plasma information across spatial, temporal, and spectral dimensions. An eight-channel X-ray focusing imaging system, operational at four-energy points (2.6, 3.1, 3.7 and 4.3 keV), was developed based on this method. By integrating this system with a streak camera, the paper successfully demonstrates the application of multiple monochromatic imaging diagnostics on imploding capsules. The subsequent sections will detail the optical and multilayers design, system assembly and adjustment, and experimental results obtained at the ShenGuang III prototype laser facility [17].

II. WORKING PRINCIPLE

Optical design

https://doi.org/10.1017/hpl.2024.30 Published online by Cambridge University Press

The X-ray focusing imaging system developed in this study is designed to capture time-evolving images of plasma spontaneous radiation across four-energy channels (2.6, 3.1, 3.7 and 4.3 keV), as well as time-integrated information such as hot spot shapes and implosion symmetry. To meet these requirements, the system is configured to acquire eight images, with two images simultaneously captured at each energy level. One image is dedicated to time-evolution imaging, and the other to time-integrated imaging. Figure 1 presents the overall configuration of the proposed system, where each set of the multilayers mirrors array comprises one total reflection spherical mirror (TRM1/TRM2) and four spherical multilayers mirrors (M1-M4) positioned sequentially along the optical axis. A single wide-spectrum TRM (either TRM1 or TRM2) is used for focusing in the meridional direction across all energy channels, while distinct spherical multilayers mirrors are utilized for spectral selection and focusing in the sagittal direction for each channel. This arrangement of spherical mirrors facilitates high efficiency and high-resolution X-ray imaging, with spectral selection achieved through four different multilayers coated on the mirrors M1-M4. This design significantly improves collection efficiency by one to two orders of magnitude over pinhole imaging, while maintaining a higher spatial resolution of 3–5 μm, and efficiently maps various image points onto the time-resolved recording device, such as a streak camera.

To ensure consistent spatial orientation of the mirrors array, given the significant variation in spatial resolution of grazing-incidence X-ray imaging with the field of view, three precision-machined reference cores were utilized, as depicted in Figure 1. The six mirrors are arranged in pairs, each aligned closely with a reference core. For the 3.7/4.3 keV energy channels, larger diameter mirrors (M1 and M2) are chosen to boost collection efficiency in the higher energy spectrum. The two total reflection mirrors (TRM1 and TRM2) each generate two columns of

https://doi.org/10.1017/hpl.2024.30 Published online by Cambridge University Press

images, which are synchronously recorded with the streak camera and image plate (IP) for concurrent time-resolved and time-integrated measurements.

Figure 1

Following the finalization of the optical schematic, the grazing angle (θ) for each spherical mirror was determined to ensure that the multilayers reflect X-rays at their respective working energies, while also reflecting the Cu Kα characteristic line (8.048 keV) for experimental assembly in an air environment using a common Cu X-ray tube. For example, TRM1 and TRM2, which primarily function at four energies, utilize multilayers coatings to reflect X-rays at 8.048 keV. Based on the total reflection condition, the grazing angles for TRM1 and TRM2 are set at 0.95°. Table 1 lists the final optical parameters of the system, including the curvature radius (R) designed to satisfy the imaging relationship shown in Equation 1 for each channel.

$$\frac{1}{u}+\frac{1}{v}=\frac{1}{f}=\frac{2}{R\sin\theta}, \tag{1}$$

where u and v represent the object and image distances, respectively, and f denotes the focus distance. The mirror lengths (d) of M1 and M2 for the 3.7 keV and 4.3 keV energy channels are set at 30 mm to enhance collection efficiency for the higher X-ray energy range.

[Table 1 here]

The system developed in this study is tailored for spontaneous imaging of X-ray emission from laser-driven plasmas at four specific energies: 2.6, 3.1, 3.7 and 4.3 keV. To ensure consistent intensity across the plasma evolution images, two sets of multilayers coatings, each operating at different grazing angles, are engineered to possess nearly identical reflectivity. The upper multilayers, designed for high reflectivity at their respective working energies, utilize Ru/C

https://doi.org/10.1017/hpl.2024.30 Published online by Cambridge University Press

materials for the low-energy channels (below 3 keV) and WC/SiC for the high-energy channels (above 3 keV). The lower multilayers, aimed at reflecting X-rays at 8.048 keV, employ a WC/SiC periodic multilayers stack. Additionally, a single-layer structure comprising W and Ni is implemented in TRM1 and TRM2 to facilitate high efficiency total reflection of X-rays below 4.3 keV. The selection of these four energies is strategic, as they are proximal to the Kα line of Cl (2.6 keV), and the Helium-like lines of Ar and Sc (3.1 keV and 4.3 keV), making them suitable for imaging diagnostics of these characteristic lines.

The multilayers were deposited on ultra-smooth silicon spherical mirrors using DC magnetron sputtering. Mirror surface roughness, measured with an AFM microscope (Bruker Dimension Icon), was maintained below 0.3 nanometers. The reflectivity curves of the multilayers at the Cu Kα line (8.048 keV) were assessed using an X-ray diffractometer (Bruker D8 plus). The multilayers parameters, including thickness, density, and interface width, were deduced by fitting the measurement data through genetic algorithm [18] with the Bede REFs software [19], as detailed in Table 2. Here, the symbol γ represents the ratio of the absorber layer (W, Si, Ru, and C) thickness to the overall period thickness. The energy response of the five spherical mirrors, based on the parameters outlined in Table 2, is depicted in Figure 2.

[Table 2 here]

Figure 2 here

In addition, to ensure that each imaging channel receives only quasi-monochromatic responses, it is crucial to employ X-ray filters to suppress low-energy rays and certain higher harmonic reflections. In this study, the selected filter combination includes 10 μm of CH, 100 μm of Be, and 2 μm of Ti. The transmission curve, as a function of X-ray energy, is depicted in Figure

https://doi.org/10.1017/hpl.2024.30 Published online by Cambridge University Press

3(a). The Be filter efficiently attenuates X-rays below 2 keV but is less effective at higher energies, while the Ti filter exhibits an absorption edge near 5 keV. The filter was placed in front of the mirrors TRM1/TRM2 to avoid the contamination and damage by the debris. Moreover, the total reflection mirrors TRM1 and TRM2 are capable of filtering out high-energy X-rays. By integrating these components, the system can effectively eliminate both low- and high-energy X-rays, thereby enhancing the monochromaticity of the imaging process. Figure 3(b) shows the combined transmission curve of four energy channels for the streak camera across the X-ray energy spectrum. Calculations indicate that the energy bandwidth is approximately 385 eV at 2.6 keV, 580 eV at 3.1 keV, 572 eV at 3.7 keV, and 440 eV at 4.3 keV. In additional, A 10μm Al filter was additionally superimposed before the time-integrated image plate (IP) to suppress brightness overexposure.

Figure 3 here

III. SYSTEM ASSEMBLY

The spatial resolution of X-ray grazing imaging optics decreases rapidly with the deviation from the central field of view. To obtain optimal spatial resolution, all mirrors of the developed system must be accurately aimed to the central field of view. Due to the diffraction effect of the grazing incidence imaging on visible light, the system assembly must be completed in the X-ray energy range. In this paper, it was completed by the imaging experiment of a metal grid using a common copper X-ray tube (8.05 keV, Cu Kα line) in an air environment. The experiment employed a 600-mesh Au grid with a period of 42 μm and line widths ranging from 5-6 μm. A marker hole with a diameter of 120 μm was predrilled on the grid to serve as an object position

https://doi.org/10.1017/hpl.2024.30 Published online by Cambridge University Press

reference. An X-ray CCD (Photonic Science VHR-11M) with pixel dimensions of 9 μm × 9 μm was positioned on the image plane to capture the imaging result for each channel. After careful adjustment of all mirrors, eight images were obtained in sequence after 10 minutes of exposure as illustrated in Figures 4(a)–(g). The operating voltage and current of copper x-ray tube are 35kV and 20mA respectively. The spatial resolution was evaluated using the "10%–90%" intensity peak-to-valley change criterion near the grid edges [20], yielding an optimal spatial resolution of approximately 3 μm in the central field of view (FOV) for each channel, while the spatial resolution within a ±100 μm FOV exceeded 5 μm. The center marker holes of the four images Figures 4(e)-(h) were arranged in a strict straight line with a two-pixel deviation, which indicated the alignment accuracy of approximately 3 μm for the same object FOV, thus these four channels were used to

Figure 4 here

couple with the streak camera to acquire one-dimensional, time-resolved image. At this time, the image spacing was 4.0 mm between 2.6 keV and 4.3 keV, 3.25 mm between 4.3 keV and 3.7 keV, and 3.6 mm between 3.7 keV and 3.1 keV. The other four channels corresponding to Figures 4(a)-(d) were used to time-integrated signal acquisition.

IV ONLINE EXPERIMENT

The four energy, eight-channel X-ray imaging system was developed for diagnostic experiments at the ShenGuang III prototype laser facility. The system's mechanical structure, depicted in Figure 5, was designed to facilitate its connection to the facility chamber and the installation of image recording components. The main flange was first connected to the facility chamber, followed by the attachment of an object point indicator, a ball with a diameter of 300

https://doi.org/10.1017/hpl.2024.30 Published online by Cambridge University Press

μm, to the multilayers mirrors array. The ball's center was calibrated to align with the position of the marker hole. Before the diagnostic experiments, the ball center could be precisely aligned using the target viewing system in the laser facility. A visible CCD was then rigidly connected to the multilayers mirrors array, enabling accurate positioning of the four image coordinates, as shown in Figure 5(b). This setup ensured precise alignment between the four image points and the photocathode of the streak camera, facilitating rapid and accurate positioning of the photocathode. Finally, an image plate (IP) was placed near the streak camera on the image plane to monitor the hot spot size, shape, and whether the streak camera is working properly.

Figure 5 here

After removing the point indicator, we placed a direct-drive CD shell target on the position of the ball's center to carry out the formal diagnostic experiment. The target shell was made of deuterated-plastic (CD) with an outer diameter of Φ = 312 μm and a wall thickness of 19.3 μm, and supported by an Au target rod. Eight laser beams (frequency tripled to 351 nm, 800 J/beam, smoothed with continuous phase plate (CPP) to Φ = 500 μm, four beams per hemisphere, equally distributed in azimuthal direction, incident angle relative to the vertical axis is 45°) directly illuminated the shell surface.

Time-resolved images of X-ray self-emission from the target at energies of 2.6, 3.1, 3.7 and 4.3 keV were captured by the streak camera, as shown in Figure 6(a). The time evolution of self-emission intensity from the CD shell target at these four energies was clearly observable. Initially, the shell surface began emitting X-rays due to laser irradiation, and as the shell underwent inward compression, the central temperature increased, resulting in further emission. The multilayers mirrors of 2.6keV and 3.1keV have the same mirror length of 10mm, but since the

https://doi.org/10.1017/hpl.2024.30 Published online by Cambridge University Press

self-emission intensity gradually decreases as the X-ray energy increases, the image brightness for 3.1keV channel was significantly weaker than 2.6keV. Despite being at a higher energy, the 3.7keV and 4.3keV channels still achieve image brightness higher than that of 2.6keV, mainly due to the longer mirror length of 30mm.

The time-integrated image recorded on the IP was presented in Figure 6(b). Due to the additional use of a 10μm Al filter to suppress overexposure, the image brightness of two low-energy channels is significantly lower than high-energy channels. According to the integrated image of high-energy channels, the center hotspot has a good symmetry indicating that the target shell was uniformly compressed.

Figure 6 here

From time-resolved images of X-ray self-emission in Figure 6, further insights into the evolution of the high-intensity emission regions on the shell surface can be gleaned, as illustrated with the mark symbols in Figure 7. Due to lower signal-to-noise ratio, the calibrated data points of the two low-energy channels at different times differ to those of the two high-energy channels. A one-dimensional (1D) hydrodynamic code laser-target coupling (LTC) [21,22] was used to simulate the imploded shell radius R and electron temperature T_e evolving with time under the current laser and target parameters, where solid lines represent the shell surfaces, color map shows the electron temperature. The figure visually represents the changes in temperature and implosion trajectory over time near the critical density surface. It is observed that there are obvious differences in the spatial distribution for different self-emission X-ray energies. The experimental measurements of high-energy emission regions (3.7keV and 4.3keV) are in good agreement with

Figure 7 here

https://doi.org/10.1017/hpl.2024.30 Published online by Cambridge University Press

the implosion trajectory predicted by theoretical simulations. The measurement results in the low-energy region (2.6keV and 3.1keV) are somewhat different from the simulation, requiring further theoretical analysis. It also illustrates the significance of the system developed in this paper.

V. SUMMARY

This study introduces a high efficiency, high-resolution multiple monochromatic imaging system for X-ray continuous self-emission diagnostics utilizing a multilayers mirrors array. An eight-channel X-ray imaging system has been designed and developed for energies of 2.6, 3.1, 3.7 and 4.3 keV, achieving a spatial resolution of approximately 3–5 μm. In conjunction with a streak camera, diagnostic experiments were conducted to analyze the temperature and implosion trajectory near critical density surfaces of a CD imploding target at the kJ-class ShenGuang III prototype facility. Compared with the previous similar system[13,14], the multilayers mirror array developed in this paper has nearly an order of magnitude improvement in collection efficiency while maintaining a spatial resolution of 3-5 μm. This system is capable of acquiring spatial, temporal, and spectral information from weak and small-scale X-ray signals during implosion, offering easily adjustable response energies with excellent scalability. This provides a novel approach for diagnosing plasma parameters in the core region of inertial confinement fusion.

Acknowledgement

This work was supported by the National Key Research and Development Program (Grant No. 2019YFE03080200), National Natural Science Foundation of China (Grant No. 12204353).

References

https://doi.org/10.1017/hpl.2024.30 Published online by Cambridge University Press

1. B. Jones, C. Deeney, J. L. McKenney, D. J. Ampleford, C. A. Coverdale, P. D. Lepell, K. P. Shelton, A. S. Safronova, V. L. Kantsyrev, G. Osborne, V. I. Sotnikov, V. V. Ivanov, D. Fedin, V. Nalajal, F. Yilmaz, I. Shrestha, "Measurement of temperature, density, and particle transport with localized dopants in wire-array Z pinches." Physical Review Letters. 100(10): 105003 (2008).
2. C. Deeney, J. P. Apruzese, C. A. Coverdale, K. G. Whitney, J. W. Thornhill, J. Davis, "Spectroscopic diagnosis of nested-wire-array dynamics and interpenetration at 7 MA." Physical Review Letters. 93(15): 155001 (2004).
3. E. L. Dewald, O. L. Landen, L. J. Suter, J. Holder, K. Campbell, S. H. Glenzer, J. W. McDonald, C. Niemann, A. J. Macknnon, M. S. Schneider, C. Haynam, D. Hinkel, B. A. Hammel, "First hohlraum drive studies on the National Ignition Facility." Physics of Plasmas. 13(5) (2006).
4. L. Yao, Y. Pu, X. Zhan, M. Wei, J. Zheng, X. Zhang, J. Yan, L.Hou, Y. Yang, Y. Ding, "X-ray fluorescence imaging of laser-driven hydrodynamic instability systems with a Ross Pair Imager." High Energy Density Physics. 37: 100882 (2020).
5. S. Z. Yi, J. Q. Dong, L. Jiang, Q. Huang, E. Guo, Z. Wang, "Simultaneous high-resolution x-ray backlighting and self-emission imaging for laser-produced plasma diagnostics using a two-energy multilayer Kirkpatrick–Baez microscope." Matter and Radiation at Extremes. 7(1) (2022).
6. M. Bitter, K. W. Hill, B. Stratton, A. L. Roquemore, D. Mastrovito, S. G. Lee, J. G. Bak, M. K. Moon, U. W. Nam, G. Smith, J. E. Rice, P. Beiersdorfer, B. S. Fraenkel, "Spatially resolved spectra from a new x-ray imaging crystal spectrometer for measurements of ion and electron temperature profiles." Review of Scientific Instruments. 75(10): 3660-3665 (2004).
7. S. Yi, H. Du, H. Si, Z. Zhou, L. Jiang, Z. Wang, R. Cheng, "Four-framed X-ray imaging crystal spectrometer for time-resolved laser plasma diagnostics." Nuclear Instruments and Methods in Physics Research Section A: Accelerators, Spectrometers, Detectors and Associated Equipment. 1057: 168722 (2023).
8. E. C. Harding, T. Ao, J. E. Bailey, G. Loisel, D. B. Sinars, M. Geissel, G. A. Rochau, I. C. Smith, "Analysis and implementation of a space resolving spherical crystal spectrometer for x-ray Thomson scattering experiments." Review of Scientific Instruments. 86(4) (2015).
9. C. Burcklen, J. von der Linden, A. Do, B. Kozioziemski, M.-A. Descalle, H. Chen, "Design of multilayer-based diagnostics for measurement of high energy x rays and gamma rays." Review

https://doi.org/10.1017/hpl.2024.30 Published online by Cambridge University Press

of Scientific Instruments. 92(3) (2021).

10. L. A. Welser, R. C. Mancini, J. A. Koch, S. Dalhed, R. W. Lee, I. E. Golovkin, F. Marshall, J. Delettrez, L. Klein, "Processing of multi-monochromatic x-ray images from indirect drive implosions at OMEGA." Review of scientific instruments. 74(3): 1951-1953 (2023).
11. H. Sawada, Y. Sentoku, T. Yabuuchi, U. Zastrau, E. Förster, F. N. Beg, H. Chen, A. J. Kemp, H. S. McLean, P. K. Patel, Y. Ping, "Monochromatic 2d k α emission images revealing short-pulse laser isochoric heating mechanism." Physical Review Letters. 122(15): 155002 (2019).
12. D. T. Cliché, R. C. Mancini, "Impact of 3D effects on the characteristics of a multi-monochromatic x-ray imager." Applied Optics. 58(17): 4753-4761 (2019).
13. S. Yi, F. Zhang, Q. Huang, L. Wei, Y. Gu, Z. Wang, "High-resolution X-ray flash radiography of Ti characteristic lines with multilayer Kirkpatrick–Baez microscope at the Shenguang-II Update laser facility." High Power Laser Science and Engineering. 9: e42 (2021).
14. S. Yi, H. Si, K. Fang, Z. Fang, J. Wu, R. Qi, X. Yuan, Z. Zhang, Z. Wang, "High-resolution dual-energy sixteen-channel Kirkpatrick–Baez microscope for ultrafast laser plasma diagnostics." J. Opt. Soc. Am. B. 39(3): A61-A67 (2022).
15. S. Yi, B. Mu, J. Zhu, X. Wang, W. Li, Z. Wang, P. He, W. Wang, Z. Fang, S. Fu, "Time-resolved multispectral X-ray imaging with multi-channel Kirkpatrick-Baez microscope for plasma diagnostics at Shenguang-II laser facility." Chinese Optics Letters. 12(8): 083401 (2014).
16. W. Wang, Z. Fang, G. Jia, S. Yi, Y. Tu, J. Zhu, B. Mu, H. An, R. Wang, Z. Xie, J. Ye, X. Meng, H. Zhou, C. Wang, A. Lei, Z. Wang, S. Fu, "Multispectral X-ray imaging with a multichannel Kirkpatrick-Baez microscope for imploded core temperature observation." The European Physical Journal D. 68: 1-5 (2014).
17. S. Jiang, F. Wang, Y. Ding, S. Liu, J. Yang, S. Li, T. Huang, Z. Cao, Z. Yang, X. Hu, W. Miao, J. Zhang, Z. Wang, G. Yang, R. Yi, Q. Tang, L. Kuang, Z. Li, D. Yang, B. Zhang, "Experimental progress of inertial confinement fusion based at the ShenGuang-III laser facility in China." Nuclear Fusion. 59(3): 032006 (2018).
18. M. Wormington, C. Panaccione, K. M. Matney, D. K. Bowen, "Characterization of structures from X-ray scattering data using genetic algorithms." Philosophical Transactions of the Royal Society of London. Series A: Mathematical, Physical and Engineering Sciences. 357(1761): 2827-2848 (1999).
19. Z. Wei, Z. Zhang, L. Jiang, Y. Yang, C. Chang, Y. Feng, R. Qi, Q. Huang, W. Yan, C. Xie, Z.

https://doi.org/10.1017/hpl.2024.30 Published online by Cambridge University Press

Wang, “Background Pressure Induced Structural and Chemical Change in NiV/B4C Multilayers Prepared by Magnetron Sputtering.” Frontiers in Physics. 10: 837819 (2022).

20. S. W. Smith, *The Scientist and Engineer’s Guide to Digital Signal Processing* (California Technical Publishing, San Diego, California,1997), p. 423–428.
21. G. Chen, T. Chang, J. Zhang, X. Zhang, W. Pei, X. You, “Numerical simulation for laser-target nonequilibrium coupling.” Chin. J. Comput. Phys. 15(4), 27–36 (1998).
22. S. Zhu, P. Gu, “Equation for laser energy deposition in laser-target interaction.” High Power Laser Part. Beams. 11(6), 687–691 (1999).

https://doi.org/10.1017/hpl.2024.30 Published online by Cambridge University Press

Figure captions

Fig. 1 Schematic representation of the high efficiency, high-resolution multiple monochromatic imaging system using a multilayers mirrors array

Fig. 2 Energy response curves for five spherical mirrors, determined through X-ray diffractometer measurements

Fig. 3 (a) Variation in filter transmittance with X-ray energy; (b) Combined transmittance curves of the four imaging channels across the X-ray energy spectrum

Fig. 4 Calibration outcomes of high efficiency, high-resolution multiple monochromatic imaging system, demonstrating its performance across four energies after assembly

Fig. 5 (a) Diagram showing the mechanical setup of the imaging system; (b) method used for precise alignment of the streak camera's photocathode using an online aiming technique

Fig. 6 Imaging results capturing X-ray self-emission from a direct-drive CD shell target at four energies: (a) captured using a streak camera; (b) recorded on an image plate

Fig. 7. Graph depicting the time-dependent variations in self-emission intensity at four energies from a direct-drive CD shell target

https://doi.org/10.1017/hpl.2024.30 Published online by Cambridge University Press

Tables

Table 1: Optical parameters of the eight-channel X-ray focusing imaging system

Mirror	E(keV)	θ	R(m)	u (mm)	v(mm)	M	d(mm)
TRM1/2	<4.3keV	0.950°	23.0	218.7	1481.3	6.773	30
M1/M2	4.3/3.7	1.320°	21.0	292.1	1407.9	4.821	30
M3/M4	3.1/2.6	1.440°	21.0	325.3	1374.7	4.297	10

Table 2: Fitted multilayers parameters of M1–M4 by X-ray diffractometer measurement

Mirror	Energy(keV)	Material	Period Number	Period Thickness (nm)
TRM1/2	<4.3	W + Ni	1	20 nm + 3nm
	8	WC/SiC	25	d = 5.05 nm，γ = 0.45
M1	3.7	WC/SiC	6	d = 8.45 nm，γ = 0.30
	8.048	WC/SiC	40	d = 3.51 nm，γ = 0.45
M2	4.3	WC/SiC	10	d = 7.00 nm，γ = 0.30
	8.048	WC/SiC	40	d = 3.51 nm，γ = 0.45
M3	2.6	Ru/C	3	d = 12.10 nm，γ = 0.50
	8.048	WC/SiC	40	d = 3.19 nm，γ = 0.45
M4	3.1	WC/SiC	3	d = 9.67 nm，γ = 0.30
	8.048	WC/SiC	40	d = 3.19 nm，γ = 0.45

https://doi.org/10.1017/hpl.2024.30 Published online by Cambridge University Press

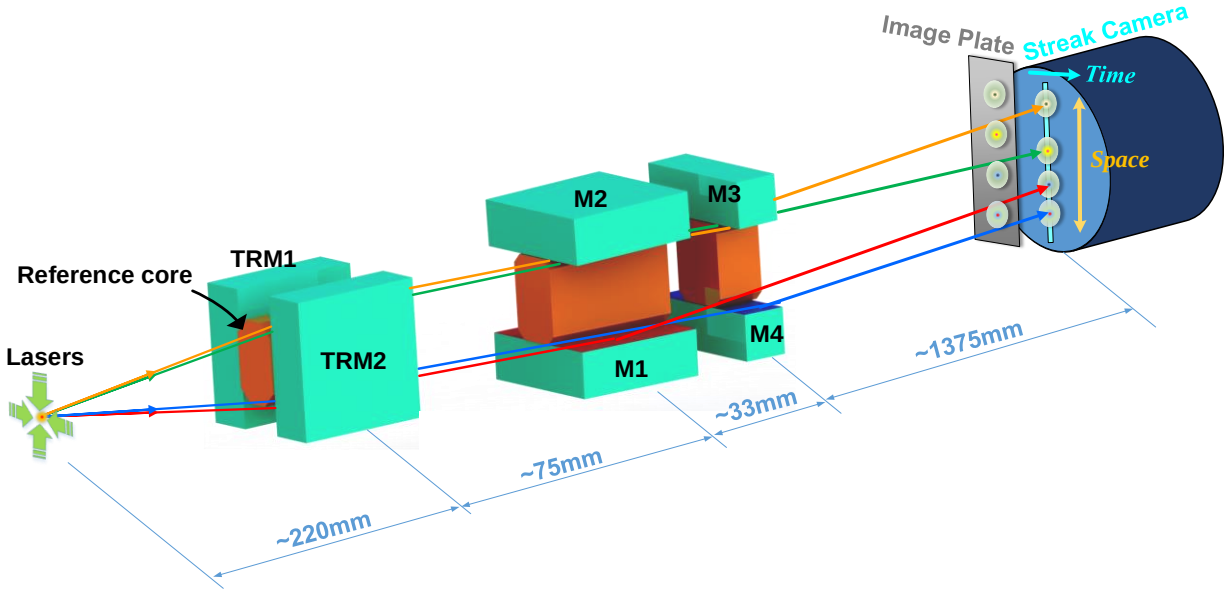

Figure 1

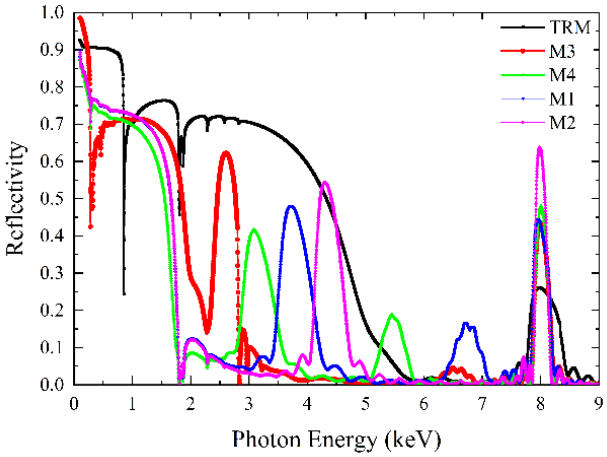

Figure 2

https://doi.org/10.1017/hpl.2024.30 Published online by Cambridge University Press

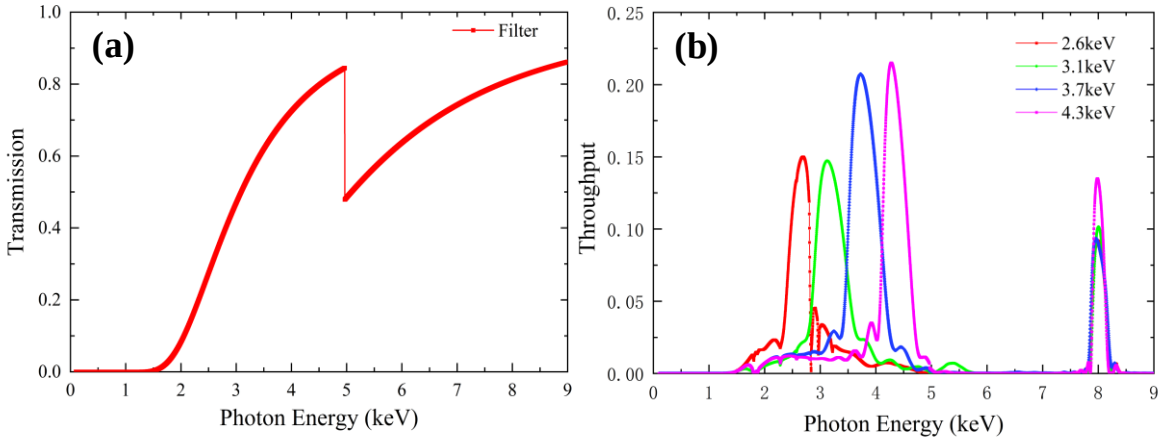

Figure 3

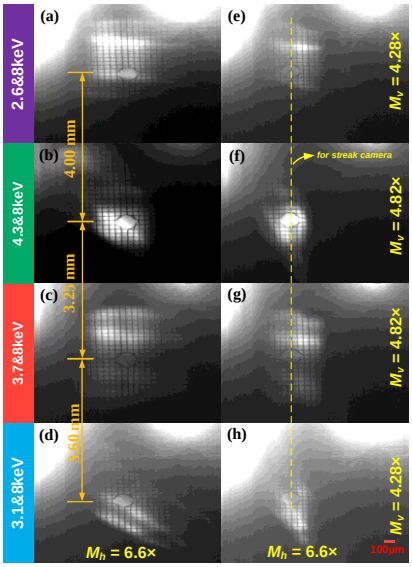

Figure 4

https://doi.org/10.1017/hpl.2024.30 Published online by Cambridge University Press

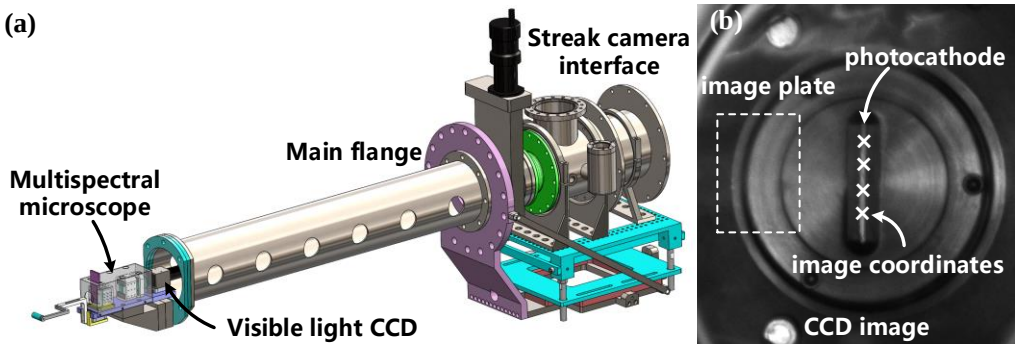

Figure 5

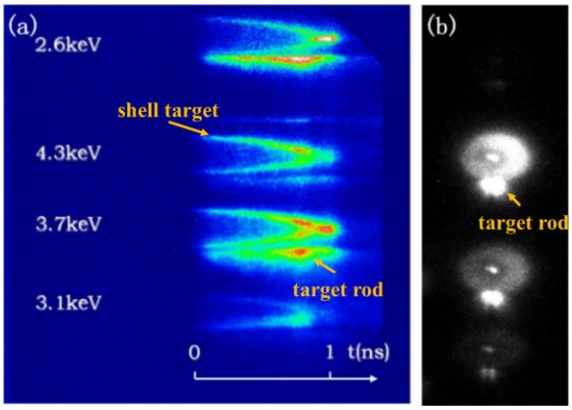

Figure 6

https://doi.org/10.1017/hpl.2024.30 Published online by Cambridge University Press

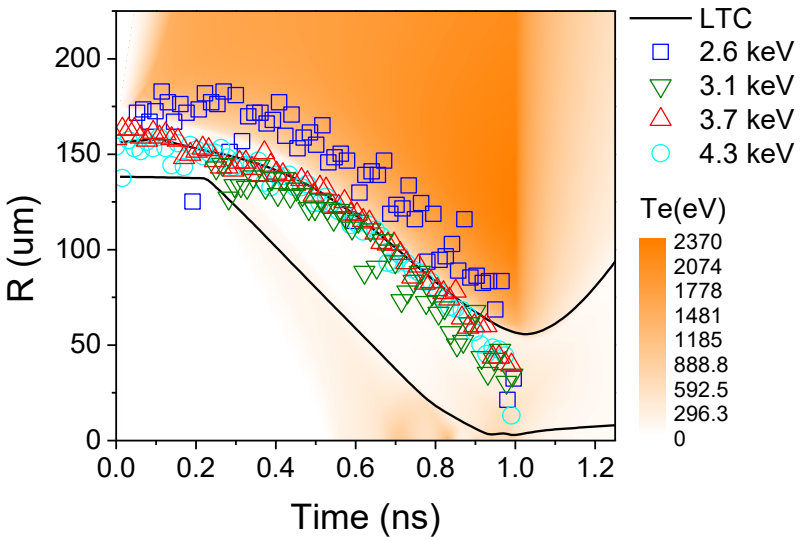

Figure 7

https://doi.org/10.1017/hpl.2024.30 Published online by Cambridge University Press